Acta Materialia 111 (2016) 138–147

Contents lists available at ScienceDirect

Acta Materialia

journal homepage: www.elsevier.com/locate/actamat

Full length article

Athermal ε-martensite transformation in a Co–20Cr alloy: Effect of rapid solidification on plate nucleation

A.L. Ramirez-Ledesma [a, *], E. Lopez-Molina [a], H.F. Lopez [b], J.A. Juarez-Islas [a]

[a] Instituto de Investigaciones en Materiales, Universidad Nacional Autonoma de Mexico, Av. Universidad 3000, Circuito Exterior S/N, Cd. Universitaria, 04510, Mexico, D. F., Mexico
[b] Materials Science and Engineering Department, CEAS University of Wisconsin-Milwaukee, 3200 N. Cramer Street, Milwaukee, WI 53211, USA

ARTICLE INFO

Article history:
Received 10 March 2016
Accepted 15 March 2016
Available online 31 March 2016

Keywords:
Cobalt based alloys
Chill casting
Rapid solidification
Martensite nucleation
Athermal ε-martensite

ABSTRACT

In the present work, a drastic increase in the formation of athermal ε-martensite was experimentally found after casting a Co–20Cr alloy in a water cooled Cu-mold. Under these conditions, rapid solidification was achieved with an alloy cooling rate of 278 K/s (approx.). The amount of precipitated athermal ε-martensite measured using X-ray diffraction was 97.26 vol. %. An inspection of the exhibited microstructure indicates that rapid solidification promotes appreciable dendrite grain refinement and alloy homogenization. In addition, the dendritic structure contained numerous visible striations associated with the athermal γ ↔ ε transformation. Transmission electron microscopy showed the development of an extremely large amount of stacking faults and stacking fault intersections, including ε-martensite plates. The microstructural characterization included an estimation of average ε-martensite plate dimensions by assuming an ellipsoidal plate geometry. These results where compared with predictions of critical ε-martensite embryo dimensions by using Eshelby's inclusion theory. In addition, a determination of the chemical volumetric free energy change, ΔG_V using a regular solution model indicated that this term is rather small. Consequently, the energy barrier for spontaneous nucleation in the Co–20Cr is relatively large when compared with other alloy systems.

1. Introduction

Co-based alloys are widely used in biomedical applications due to their excellent corrosion resistance, wear and mechanical properties [1,2]. These properties are intimately related to the relative amounts of γ-FCC (face centered cubic) and ε-HCP (hexagonal close-packed) phases present in the alloy. From the Co-Cr binary system, it is found that phase equilibria between γ-Co and ε-Co in the Co-rich region occurs at 1073.15 K (800 °C), Fig. 1. Below this temperature, the thermodynamically stable phase is expected to be HCP ε-Co [3]. Nevertheless, the γ ↔ ε transformation is severely limited by nucleation events, which give rise to faulting [4]. Consequently, in most conventionally solidified Co-Cr-Mo-C alloys the γ-Co FCC-phase is retained at room temperature [5–7]. Apparently, the γ-FCC → ε-HCP transformation is extremely sluggish under conventional solidification conditions due primarily to limited chemical driving forces available at the transformation temperature [5–7].

In cobalt alloys, the martensitic transformation can be induced by (1) athermal, (2) isothermal and (3) strain induced mechanisms [5,8–12]. In particular, in athermal transformations the amount of transformed martensite depends primarily on the quenching temperature and not on the residence time at this temperature. Experimentally, it has been found that in conventionally solidified Co-Cr-Mo-C alloys the reported amounts of athermal ε-martensite are relatively small, not exceeding 20 vol. % in most cases [6,13]. The limited extent of athermal martensite induced in Co-Cr-Mo alloys has been attributed to the lack of enough defects necessary for the spontaneous formation of ε-embryos during alloy cooling from the γ-phase.

The work by Olson and co-workers [14] has shown that when the alloy stacking fault energy (γ_{SF}) becomes zero or negative ε-martensite embryos can be formed spontaneously. The nucleation defect being a faulting mechanism consisting of a group of lattice dislocations where the motion of a Shockley partial on every second FCC closed packed plane gives rise to an ε-phase nucleus.

---

* Corresponding author.
E-mail addresses: alramirez.unam@gmail.com (A.L. Ramirez-Ledesma), eduardolm@comunidad.unam.mx (E. Lopez-Molina), hlopez@uwm.edu (H.F. Lopez), julioalb@unam.mx (J.A. Juarez-Islas).

http://dx.doi.org/10.1016/j.actamat.2016.03.047
1359-6454/

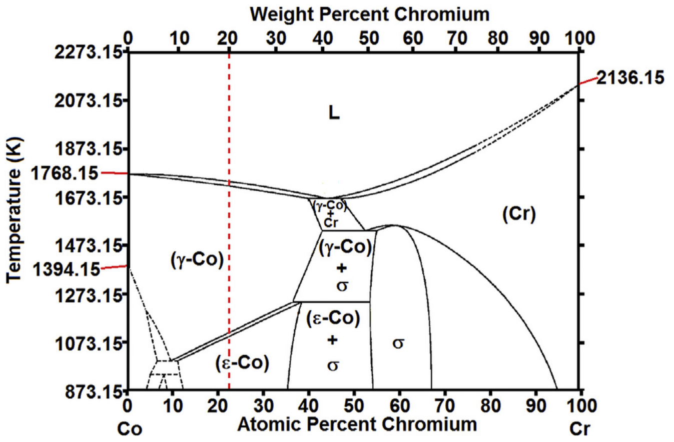

Fig. 1. The Co–Cr binary phase diagram.

Among the possible faulting defects suggested are tilt boundaries, twin intersections, incoherent twins or inclusion interfaces [14,15]. Yet, the estimated density of the proper faulting defects is of the order of 10^5–10^7/cm^3, which explains the sparse amounts of precipitated athermal martensite in cobalt based alloys [14].

In the work of Olson and Cohen [14], the effect of rapid alloy solidification was not considered. Nevertheless, there are reports that indicate that in Co-based alloys the athermal martensitic transformation is strongly promoted by rapid solidification from the melt [16–20]. Accordingly, in this work, the effect of rapid solidification on the athermal ε-martensite transformation is investigated in a Co–20Cr alloy. In particular, this work is aimed at disclosing the microstructural conditions which give rise to appreciable nucleation of athermal ε-martensite embryos when chill casting conditions are imposed.

In addition, the basic concepts of classical nucleation are considered in identifying conditions for spontaneous embryo formation. In this case, the crystallographic features of the martensite transformation are accounted for by including a Bain distortion and Eshelby's inclusion treatment [21]. The energetics of the proposed mechanism is then used in defining critical geometrical parameters for the formation of a spontaneous martensite embryo. The predictions of the proposed analysis are then compared with experimental determinations based on scanning and transmission electron microscopy of embryo dimensions in athermally nucleated ε-martensite.

1.1. *Athermal nucleation*

In the work of Olson and Cohen [14], the classical nucleation theory was used in identifying energetic conditions for the spontaneous nucleation process of martensite embryos. In their work, the critical condition for spontaneous embryo nucleation was taken to be $\gamma_{SF} = 0$. In addition, the critical embryo size was given in terms of the number of dissociated lattice dislocations in the inclusion. In the proposed analysis, minimal energy conditions for embryo nucleation were found as a function of the embryo geometry (size and thickness) by using the method proposed by Easterling and Thölén [21]. In this method, the energy considerations for the austenite-martensite transformation are defined by the well-known Eshelby formalism [22].

Consider a martensite embryo plate (such as the ones found in the directionally solidified Co–20Cr alloy) which is expected to nucleate upon cooling. Energetically, various workers [14,21] have suggested that martensite nucleation from a defect occurs as a result of the propagation of existing strain fields rather than energy consumption by the phase change. In this context, the structural defects capable of acting as nucleation sites must possess long range stress fields [14]. Among the reported faulting defects that promote embryo nucleation are incoherent twin boundaries, grain boundaries and incoherent inclusion particles [15,23].

In addition, consider a Bain distortion which gives rise to martensite from the austenitic matrix with a minimum of atomic displacements and an invariant plane condition. In the case of a small inclusion, lattice invariant deformation might not be required as the inclusion is under the strain field of a defect. Accordingly, the total energy associated with the nucleation process is given by Ref. [21].

$$E_{tot} = E_{surf} + E_{strain} + E_{chem} + E_{int}. \tag{1}$$

Notice that the total energy incorporates (a) the coherent interfacial energy between the austenite matrix and the martensite embryo (E_{surf}), (b) coherency strains due to a change in lattice parameters (E_{strain}), (c) the difference in chemical free energy for the austenite-martensite transformation (E_{chem}) and (d) interaction between the strain field of a Shockley partial and the strain field of the martensite embryo (E_{int}). Since ε-martensite embryos result from the dissociation of a number of properly spaced lattice dislocations, the development of stable nuclei is then plausible whenever a net energy reduction occurs through the incorporation of a dissociated dislocation onto the critically sized martensite embryo.

Considering the geometry for martensite nuclei assumed by Easterling and Thölén [21] and by Olson and Cohen in Ref. [24], a single martensite embryo possessing a thin ellipsoidal geometry can be defined by a semi-thickness c, a radius a and volume V. The thin ellipsoidal geometry for the martensite embryo is shown in Fig. 2. This figure also contains a top view of the ellipsoidal embryo which resembles a flat plate, as well as a front view resembling a needle-shaped inclusion. In addition, it is assumed that the transformation can be expressed by a simple shear of magnitude S and that the interaction of the strain field of the Shockley partial is compatible with the strain field of the martensite embryo. Under these assumptions, Eq. (1) can be rewritten as [21].

$$E_{tot} = 2\pi\sigma a^2 + \frac{\pi\mu}{2}\left(\frac{S}{2}\right)^2\frac{(2-\upsilon)}{(1-\upsilon)}\frac{c}{a}V - \Delta G_V V - \frac{\pi^2\mu Sb}{4}\frac{2-\upsilon}{1-\upsilon}ac, \tag{2}$$

In the above expression, the total energy is a function of the surface energy (σ), the shear modulus of the austenite matrix (μ),

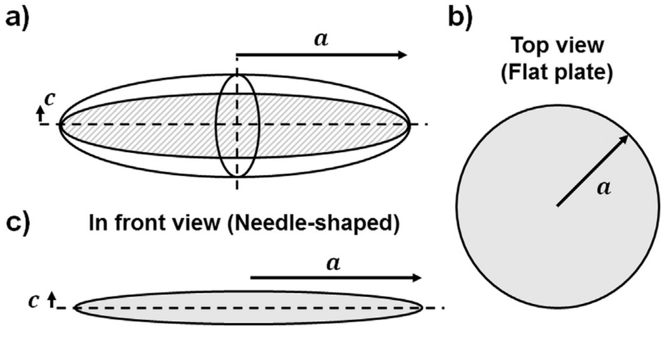

Fig. 2. (a) Martensite embryo with thin ellipsoidal geometry, c and a corresponds to semi-thickness and radius, respectively, (b) Top view for martensite embryo that resembles a flat plate, (c) In front view for martensite embryo that resembles a needle-shaped morphology.

Table 1
Selected alloy properties.

Property	Value in I.S. units	Reference
S	0.2	[21]
σ	0.0075 J/m^2	[28]
μ	8.8×10^{10} Pa	[28]
υ	0.28	[28]
b	0.145×10^{-9} m	[28,29]
ΔG_V	2.098×10^6 J/m^3	–

Table 2
Computed ΔG_V, energy barrier values and critical parameters for athermal martensite nucleation in selected alloys.

Alloy [reference]	ΔG_V [J/m^3]	Energy barrier [J]	c [nm]	a [nm]
Co–20Cr	2.098×10^6	5.692×10^{-12}	6.953	20176
Co–29Cr–6Mo [28,30]	7.801×10^6	6.065×10^{-15}	1.652	938.84
Steel [21,31]	1.740×10^8	6.650×10^{-16}	2.044	53.331

Poisson's ratio (υ), the volumetric chemical free energy difference (ΔG_V) and the magnitude of the Burgers vector intrinsic to the Shockley partial (b). The value of σ used is minimum as it corresponds to a fully coherent interface, but increases as the interface becomes semi-coherent. According to various workers, in transition metals and alloys the value of σ varies from 0.005 to 0.015 J/m^2 [25,26]. In addition, the magnitude of μ is of the order of 10^{10} Pa [27] whereas υ is around 1/3 [21].

The shear transformation can be determined by the strain over the inclusion; in this instance, the various parameters used in Eq. (2) are given in Table 1. The total energy associated with the athermal martensite embryo was estimated using the data reported by Yamanaka and co-workers for a Co–29Cr-Mo alloy [28] (see Table 2). Moreover, ΔG_V is highly sensitive to the molar weight of the elements involved, as well as, to the austenite-martensite transformation temperature, Hence, in this work a determination of ΔG_V is made by considering a regular solution model as described in Appendix A.

Fig. 3 shows the total energy surface contour predicted by Eq. (2) by arbitrary varying the c and a geometrical martensite plate parameters. From this graph, minimal energy conditions required for embryo nucleation can be found including critical parameters that satisfy minimal energy conditions (as described in the minimal energy subsection). In addition, Fig. 3 shows the critical dimensions needed for martensite nucleation from an austenitic matrix in other alloy systems.

1.2. Minimal energy

Minimal energy conditions necessary to surmount the energy barrier for nucleation can be estimated by a partial derivation of Eq. (2) [21] with respect to the a and c parameters. As a result of this derivation, a system of two coupled equations is obtained, which can be described by the array in Eq. (3). In this expression, each partial derivation evaluated for the critical parameters c_{crit} and a_{crit} must be equated to zero. The equations for the critical parameters obtained by this method thus provide the semi-thickness and radius that satisfy the minimal energy state. A minimal energy expression can then be obtained by substitution of the critical parameters c_{crit} and a_{crit} into the energy equation (Eq. (2)).

$$\begin{cases} \left.\dfrac{\partial}{\partial c} E_{tot}(a,c)\right|_{\substack{c = c_{crit} \\ a = a_{crit}}} = 0 \\ \left.\dfrac{\partial}{\partial a} E_{tot}(a,c)\right|_{\substack{a = a_{crit} \\ c = c_{crit}}} = 0 \end{cases} . \tag{3}$$

In the case when there is no interaction between the strain field of the Shockley partial dislocation and the strain field of the martensite embryo (E_{int}=0), critical parameters that satisfy Eq. (3) are given by Eqs. (4) and (5).

$$c_{crit} = \frac{2\sigma}{\Delta G_V}, \tag{4}$$

$$a_{crit} = \frac{5\pi\sigma\mu}{(\Delta G_V)^2}\left(\frac{S}{2}\right)^2. \tag{5}$$

Under these assumptions, the minimal energy condition can be described by the expression proposed by Easterling and Thölén [21].

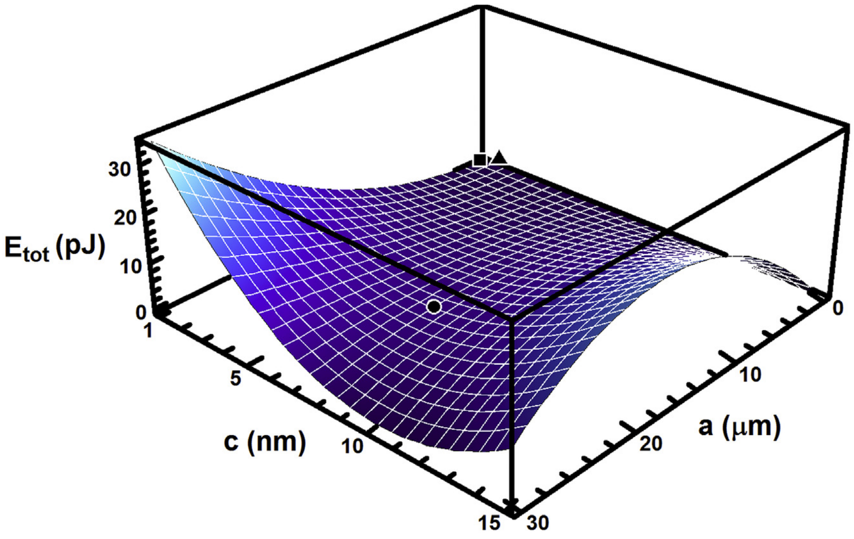

Fig. 3. Energy surface generated by arbitrary variation of c and a plate dimensions in Eq. (3). Minimal energy conditions for the Co–20Cr alloy, a Co–29Cr–6Mo alloy and a Fe–Cr–Ni steel are marked by a circle, a square and a triangle, respectively.

Table 3
Computed critical parameters (*c* and *a*) and critical energy contributions for an ellipsoidal plate in the Co–20Cr alloy. Energy units are expressed in pJ.

Condition	*c* [nm]	*a* [μm]	E_{surf}	E_{strain}	E_{chem}	E_{int}	E_{tot}
$E_{int}=0$	7.150	23.553	26.143	16.654	−34.857	0	7.940
$E_{int}\neq 0$	6.953	20.176	19.183	13.492	−24.873	−2.110	5.692

$$E_{min} = \frac{50\pi^3}{3}\frac{\sigma^3\mu^2}{(\Delta G_V)^4}\left(\frac{S}{2}\right)^4. \tag{6}$$

Alternatively, in the case of interaction between the strain field of the partial dislocation and the strain field of the martensite embryo ($E_{int}\neq 0$), minimal energy and critical size parameters do not have general analytic expressions equivalent to Eqs. (4) and (5). When $E_{int}\neq 0$, critical parameters are obtained by numerical substitution of all constants involved in the system given by Eq. (3). To ensure an accurate calculation, a solution to the system of coupled equations was obtained by using the Wolfram Mathematica® software. The results of minimal energy computations are given in Table 3. The first column refers to no interaction whereas the second column considers the effect of strain field interactions. The computed energies were calculated for the critical plate dimensions determined in this work (see 1.1. athermal nucleation subsection) and they are also given in Table 3.

An important result of the above analysis (see Table 3) indicates that the elastic field interactions between the Shockley partial and the martensite embryo leads to a net reduction in the surface and strain energy contributions to martensite embryo nucleation. In turn, a reduction in the total energy barrier for nucleation of around 2.270 pJ implies that nucleation is highly favored by the propagation of the interacting elastic fields. Thus, the spontaneous nucleation of athermal ε-martensite is assisted by further dissociation of partial dislocations. Table 3 summarizes the outcome on computed chemical volumetric free energies, critical energy barriers and the martensite plate dimensions, *a* and *c*.

2. Experimental

High purity cobalt (99.99%) and chromium (99.99%) were used as starting metals for processing the experimental Co–20 wt. % Cr alloy. The alloy was processed by vacuum induction melting under an argon (Ar) atmosphere. In order to avoid melt contamination alumina crucibles were used for alloy casting [32]. The foundry process consists of three vacuum times, each of twenty minutes prior to melting. Along with the three vacuums, argon purges were implemented to remove any residual oxygen inside the furnace.

Subsequently, the liquid metal was brought to a temperature above 2200 K (1926 °C approx.), to ensure the complete dissolution of chromium (Cr). Finally, the liquid alloy was poured at a temperature of 1873.15 K (1600 °C) in a Cu-mold coupled with a cooling system where water is recirculating at all times during melting and in the casting process, (Fig. 4 (a)). In turn, this enabled the temperature of the cooper mold to remain always at around 298.15 K (25 °C). A cooling rate of the order of 278 K/s was achieved at the time of casting. The temperature profile for these cooling conditions (Fig. 4(b)) was recorded using an Amprobe TMD90A Digital Thermometer with R type thermocouples inserted into a ceramic sheath, embedded in the cooling metal.

Plates of 10 cm × 5 cm × 7 mm were cast and the developed phases were identified and quantified by X-ray diffraction in a Siemens D-5000 diffractometer using Kα-Cu (1.5418 Å) radiation. Metallographic preparation was achieved by grinding all the way to 2000 grit paper followed by polishing with 1 μm alumina slurry. Electrolytic etching at 6 V and 5 mA for 20 s using a 60 vol. % HNO_3 + 40 vol. % H_2O solution revealed the alloy microstructure. The as-cast microstructure was examined by scanning electron microscopy (SEM) in a JEOL-7600f microscope coupled with an energy dispersed X-ray microanalysis (EDS). Thin foils for transmission electron microscopy (TEM) were prepared using a Struers Tenupol 2 3 5 Twin Jet Electro Polisher in a 60 vol. % HNO_3 + 40 vol. % H_2O solution as electrolyte. A JEOL-TEM operating at 120 kV was used for observations of selected area electron diffraction (SAED) patterns.

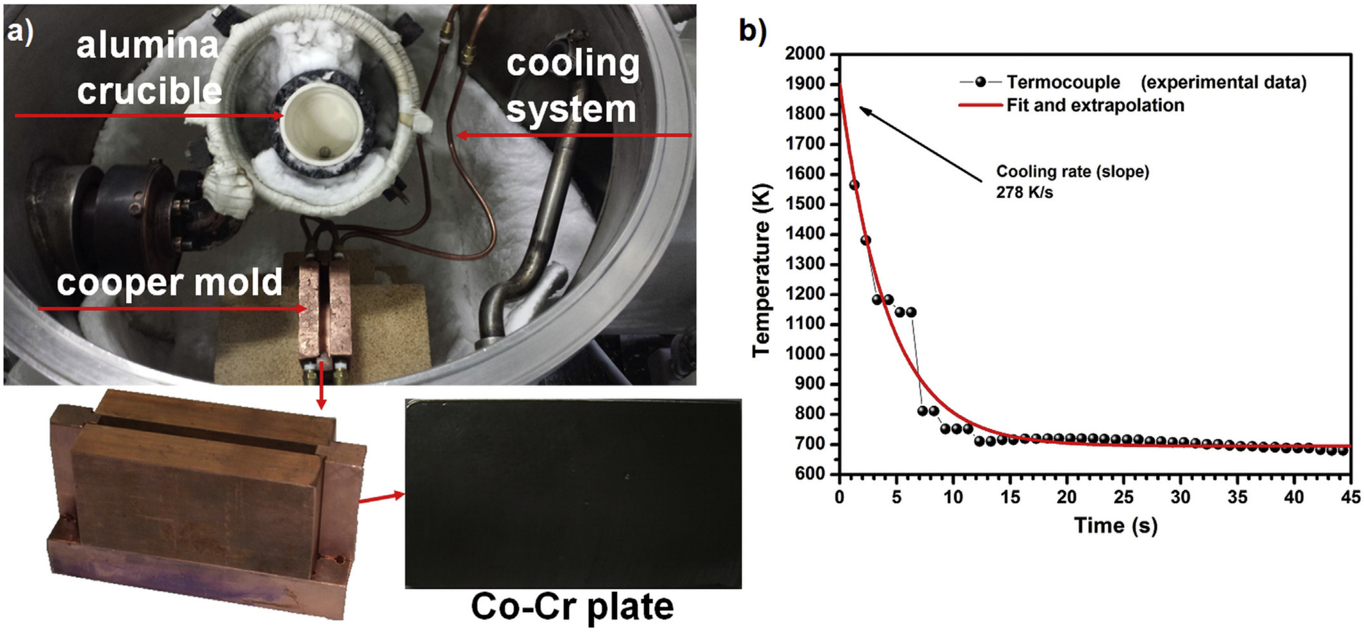

Fig. 4. (a) Scheme of the casting process showing the cooper mold coupled with the cooling system where water (298.15 K) is recirculating all the time during melting and casting and, the Co–20 wt. % Cr alloy plate. The unidirectional heat flux is in the x-direction perpendicular to cast direction, (b) Temperature profile (black curve: experimental data, red curve: fit and extrapolation). (For interpretation of the references to color in this figure legend, the reader is referred to the web version of this article.)

3. Results

3.1. X-ray diffraction

Fig. 5 shows X-ray diffraction peaks for the as-cast directionally solidified Co–20Cr alloy. Notice that the first (111) and second (200) diffraction peaks corresponding to the γ-FCC phase appear at 2θ values of 44.74° and 52.74°, respectively. Also, notice that the $(10\bar{1}0)$, (0002) and $(10\bar{1}1)$ HCP ε-phase peaks are found at 41.5°, 44.74° and 47.37° 2θ values, respectively. For determinations of athermal ε-martensite the method proposed by Sage and Guillaud [33] was employed using the expression.

$$HCP\ (wt.\%) = \frac{I\left(10\bar{1}1\right)_{HCP}}{I\left(10\bar{1}1\right)_{HCP} + 1.5\,I(200)_{FCC}}, \tag{7}$$

where $I(200)_{FCC}$ and $I(10\bar{1}1)_{HCP}$ are the integrated intensities of the $(200)_\gamma$ and $(10\bar{1}1)_\varepsilon$ diffraction peaks for the FCC and HCP phases, respectively. The relative intensities and the amount of athermal ε-martensite in the Co–20Cr alloy are given in Table 4. In particular, notice a dramatic increase in the amount of transformed athermal ε-martensite which approaches 100% (97 vol. %) induced through rapid solidification. In addition, the γ-Co (FCC) and ε-Co (HCP) lattice parameters were calculated using Bragg's law and the corresponding crystallographic expressions for interplanar spacings [34]. For the FCC phase, lattice parameter determinations were based on the average values found for the (111), (200), (220) and (311) peak positions, whereas the $(10\bar{1}0)$, (0002) and $(10\bar{1}1)$ peaks were used for the HCP-phase.

It is well known [8] that coherent growth in the Bain distortion as represented in Fig. 6 includes two mechanisms: (a) an invariant axis trough coherent growth and, (b) a contraction and expansion in the other lattice axes. In Co-based alloys, the martensitic transformation shows an invariant plane along the [111] and [0002] axes for the γ-FCC and ε-HCP phases, respectively [25]. In turn, this implies that the magnitude of the c_{HCP} lattice parameter should equal 2/3 the main diagonal of the FCC unit cell. From the X-ray diffraction data (see Fig. 5), the estimated lattice parameters are a_{FCC} = 3.46443 Å and c_{HCP} = 3.92099 Å for the as-cast Co–20Cr alloy. From this outcome a contraction along the c-axis (i.e. normal to the basal plane) of around 1.98% was found which can be associated with additional strain contributions to the coherency strain when the martensitic transformation occurs.

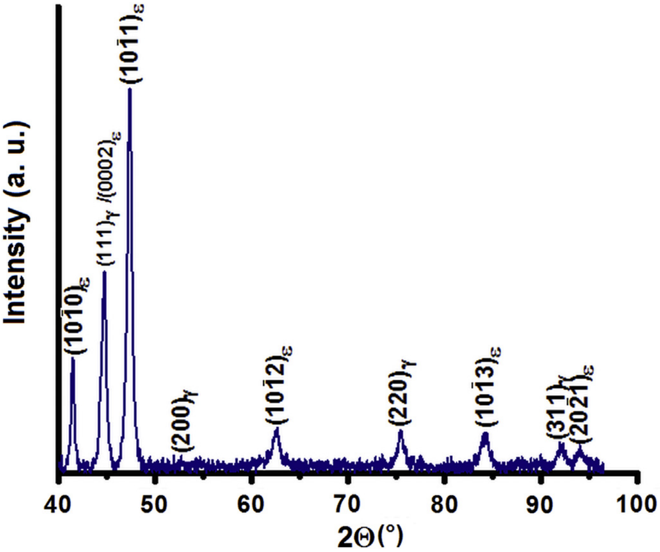

Fig. 5. X-ray diffraction pattern of the as-cast directionally solidified Co–20Cr alloy cooled at 278 K/s.

Table 4
Relative X-ray intensities and vol. pct. ε-martensite in the Co–20Cr alloy.

Alloy	HCP (vol. %)	$I(10\bar{1}0)_{HCP}$ [u^2]	$I(200)_{FCC}$ [u^2]
Co–20 Cr	97.26	464.61	8.71

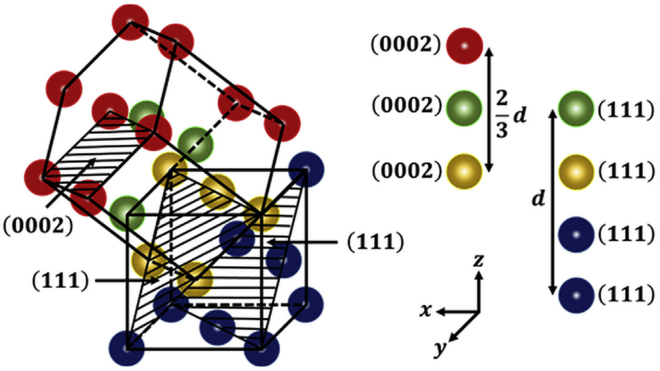

Fig. 6. Schematic illustration of coherent growth between γ-FCC and ε-HCP phases in the austenite-martensite transformation. Notice the relationship between the c_{HCP} lattice parameter and the major diagonal in the FCC unit cell.

3.2. Microstructural features

Fig. 7 is an SEM micrograph of the columnar dendrites developed by directional solidification showing 001 preferential orientation. Notice the vast amounts of martensite as evidenced by the supersaturated arrays of straight transgranular markings known as striations. These striations, typical of athermal ε-martensite are found inside the columnar dendrites. Moreover, this figure schematically shows the dissociation of a lattice dislocation $\frac{1}{2}[\bar{1}01]$ into its Shockley partial components $\frac{1}{6}\bar{1}\bar{1}2$ and $\frac{1}{2}[\bar{2}11]$ along closest packing (111) planes [35] as anticipated in the dendritic structure.

Detailed features of some of the plausible ε-martensite nucleation sites were disclosed by TEM observations. Fig. 8 shows a large density of stacking faults, including a large number of athermal ε-martensite plates (Fig. 8 (a)) [5] and coherent interfaces between the γ-FCC/ε-HCP phases (Fig. 8 (b)) [21]. In particular, Fig. 8 (a) shows the formation of athermal ε-martensite from the austenite phase in the region labeled "γ/ε". The exhibited morphology of the athermal ε-martensite is consistent with the HCP_1 phase reported by K. Rajan [36].

From the electron diffraction pattern (Fig. 8 (c)) taken in the area labeled (2), it is found that the zone axis for the HCP ε-Co is $[01\bar{1}0]$. Also, in the area (1) (see Fig. 8 (b)) both γ-FCC and ε-HCP phases are present with zone axes [011] and $[01\bar{1}0]$, respectively. These phases exhibit a $(11\bar{1})||(0002)$ orientation relationship. In addition, randomly orientated athermal ε-marteniste is shown in the bright field micrograph of Fig. 9 (a) which includes a large amount of stacking faults, stacking fault intersections and martensite plates.

Fig. 9(b–c) are the corresponding dark-field images of the selected areas (1) and (2), respectively. The corresponding diffraction pattern is shown in Fig. 9 (d), with a zone axes for the ε-Co, HCP phase [0001]. The exhibited features of a high density of stacking faults in these microstructures are analogous to the ones reported by Zhuang and Langer [37] for a rapidly cooled Co-Cr-Mo alloy.

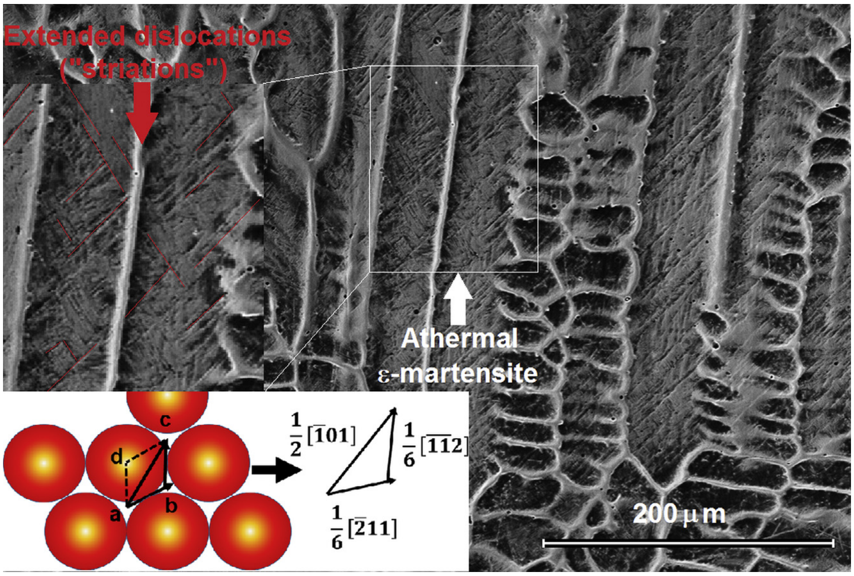

Fig. 7. SEM micrograph of the as-chill cast Co–20Cr alloy showing a vast martensitic transformation including typical athermal ε-martensite striations within columnar dendrites. It also shows the dislocation dissociation reaction: $\frac{1}{2}[\bar{1}01]\rightarrow\frac{1}{6}[\bar{1}\bar{1}2]+\frac{1}{6}[\bar{2}11]$.

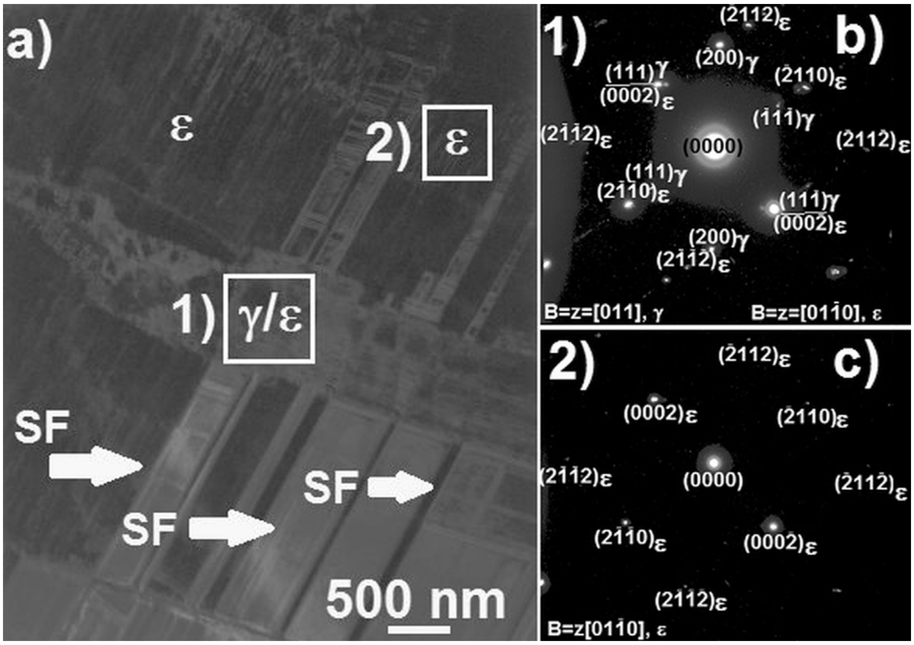

Fig. 8. (a) Bright field micrograph of the as-cast Co–20Cr alloy showing several features related with a high percentage of ε-martensite transformation: a large density of stacking faults (SF), fine athermal ε-martensite plates and coexistence between γ-FCC/ε-HCP phases (diffraction pattern 1), (b) Diffraction pattern of zone labeled as 1 showing a $(11\bar{1})||(0002)$ orientation relationship, (c) Diffraction pattern of zone labeled as 2 showing the ε-HCP indexing with a zone axes $[01\bar{1}0]$.

4. Discussion

H. Jones [38] has described conditions for rapid solidification in alloys systems. In his work he indicated that cooling rates exceeding 10^2 K/s fall in the range of rapid solidification. Accordingly, from the experimentally determined cooling curve exhibited by the Co- 20 wt.% Cr alloy in this work, it is evident that the alloy is in the regime of rapid solidification (278 K/s, Fig. 4 (b)).

From Fig. 5, an estimation of the amount of transformed athermal ε-martensite in the directionally solidified Co–20Cr alloy gives 97 vol.% ε-martensite. Since the γ ↔ ε transformation is intimately related to the ability of a stacking fault to extend indefinitely, this process is strongly dependent of the local variations in γ_{SF} with the solute content of these faults [30]. In this regard, a clear advantage of employing rapid solidification is the elimination of any detrimental effects associated with interdendritic segregation. Fig. 10 shows and SEM micrograph and corresponding X-ray mapping of chromium in a region of a directionally solidified columnar dendrite. Notice that Cr is uniformly distributed with no evidence for solute (Cr) segregation in the interdendritic regions of the investigated alloy.

In cobalt based alloys, the athermal martensite formation is

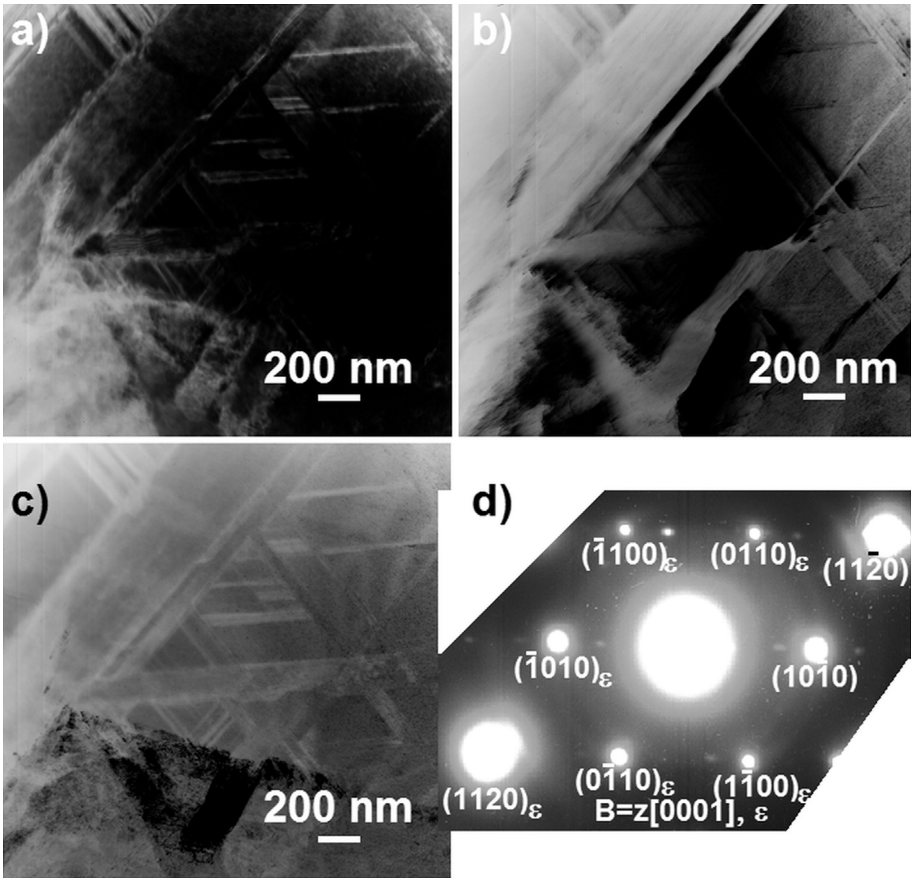

Fig. 9. (a) Bright field micrograph of a Co–20Cr alloy showing martensite plates randomly distributed, (b) and (c) are dark-field images of selected areas 1) and 2) respectively. (d) Selected-area electron diffraction pattern with zone axis $[0001]_\varepsilon$.

expected to occur by a diffusionless mechanism. Yet, the nucleation stage during the transformation is limited by the availability of faulting defects such as intrinsic stacking faults. In the work of Olson and Cohen [14] the critical condition for the spontaneous formation of athermal martensite embryos is satisfied when $\gamma_{SF} = 0$. In addition, martensite nucleation from faulting defects can be considered as a heterogeneous process closely linked to the propagation of strain fields between the martensite embryo and the nucleation defect.

In this work, it is found that rapid solidification introduces a high density of fault defects including twins, stacking faults and grain boundaries in agreement with other reports [5,38–40]. Moreover, non-equilibrium cooling from elevated temperatures generate local vacancy supersaturations around lattice dislocations [30]. In turn, these high local vacancy supersaturations can give rise to osmotic forces on the dislocations [35]. These forces are tremendously high and can easily modify the dislocation substructure through various dislocation–vacancy interactions including climbing and the development of dislocation loops. In addition, condensation of excess vacancies along closed packed FCC planes can lead to the development of prismatic vacancy loops which resemble intrinsic stacking faults except for the nature of the burgers vector (Frank partial dislocations). Intrinsic stacking faults have been considered as potential fault defects for the spontaneous nucleation of athermal martensite embryos [14].

A large density of stacking faults and of ε-martensite plates is

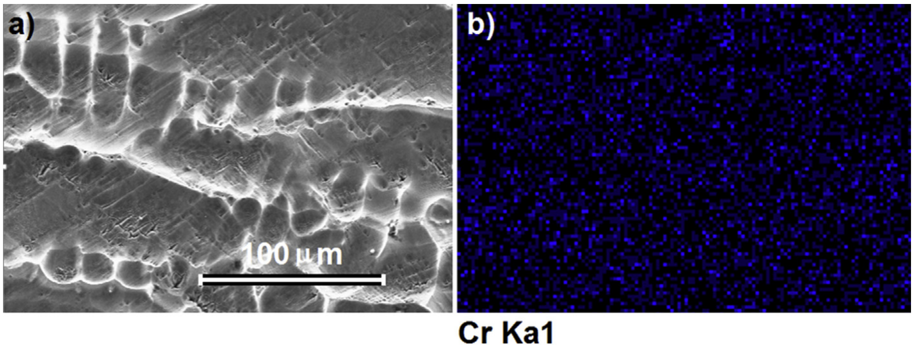

Fig. 10. (a) SEM micrograph of the as-chill cast Co–20Cr alloy showing a part of columnar dendrites directionally solidified, (b) X-ray mapping of Cr (chromium).

found in this work due to rapid solidification. This strongly indicates that the density of fault defects which promote spontaneous embryo formation is drastically enhanced, well beyond the ones reported by Olson and Cohen (10^5–10^7 per cm^3) [14]. From this work, it is evident that a full $\gamma \leftrightarrow \varepsilon$ transformation in cobalt based alloys is highly possible when fast cooling rates are implemented such as in rapid solidification processing. The large amounts of transformed martensite agree with the experimental outcome from other workers [5,37] of an increasing density of dissociated dislocations combined with stacking faults and stacking fault intersections in fast-cooled Co-based alloys.

In the investigated alloy, additional lattice straining is experimentally found when the $\gamma \leftrightarrow \varepsilon$ transformation occurs. These strains consist mainly of a contraction normal to the basal plane of approximately 1.8 pct. Thus, there is an additional contribution of coherency energy to the fault energy (E_{strain}) which arises from these strains (beyond the ones due to the existing dislocations) and that are needed to complete the transformation to the product lattice. In the work of Olson and Cohen [14], an estimation of the strain energy contribution of a 1 pct. contraction in Fe–Cr–Ni alloys along the hcp c axis yields a value of 42 J/mol which is significant. Nevertheless, this energy contribution is expected to monotonically decrease as the embryos widen along the fault plane. This process is accomplished with increasing separation of the partial dislocations. Once the conditions described by Eq. (6) are satisfied, spontaneous formation of a martensite embryo occurs. Notice from Eqs. (4) and (5) that in the investigated Co–20Cr alloy that the nucleated plate length is relatively large when compared with the ones predicted for other systems (see Table 2). This effect can be attributed to the relatively large c axis contraction (1.8 pct.) which is expected to increase the contribution of coherency energy by almost two fold when compared with the one estimated by Olson and Cohen [14].

Determinations of martensite plate dimensions a and c were made by SEM and TEM means. Fig. 11 (a) shows the length of athermal ε-martensite as resolved by SEM means. Inasmuch as this length is delimited by striations that correspond to the extended dislocations which enclose several martensite plates. Since the plane of the examined alloy surface will cut martensite plates at different locations, a distribution of plate lengths is found as shown in Fig. 11 (b). Notice from this Figure, that plates are located on the largest length range (37–42 μm). Because of the high occurrence probability that accompanies the statistical mode, length measurements on this region can be used to estimate a representative length for martensite plate. The average plate length obtained is 40.952 ± 2.875 μm, this value is in good agreement with the one predicted by the proposed analysis (see Fig. 2 and Table 3). Martensite plate thickness cannot be resolved in the SEM and further work was carried out using transmission electron microscopy for thickness determinations.

Fig. 12 shows an area containing a copious number of martensite plates aligned in a preferential direction. From this figure, the thickness of athermal ε-martensite plates is clearly visible making it possible to make measurements directly in the TEM yielding values of approximately 13.793 nm (this corresponds to the $2c$ value). A comparison of the experimentally measured plate dimensions $2a$ (40.352 μm) and $2c$ (13.906 nm) with the predictions based on minimal energy conditions for spontaneous embryo nucleation yield errors of only 1.486% and 0.812%, respectively (see Table 3). The slight variations between the experimental evidence and the theoretical predictions may be attributed to oversimplification in the computed calculations as more detailed expressions for the energy barrier components and corresponding critical parameters require increasingly complex interactions that are not included in Eshelby's inclusion treatment. Notice that these estimations assume that during the athermal transformation, martensite nucleation is dominant whereas growth is severely hindered. In particular, from this outcome the density of nucleating fault defects can be estimated by considering a mean plate volume of

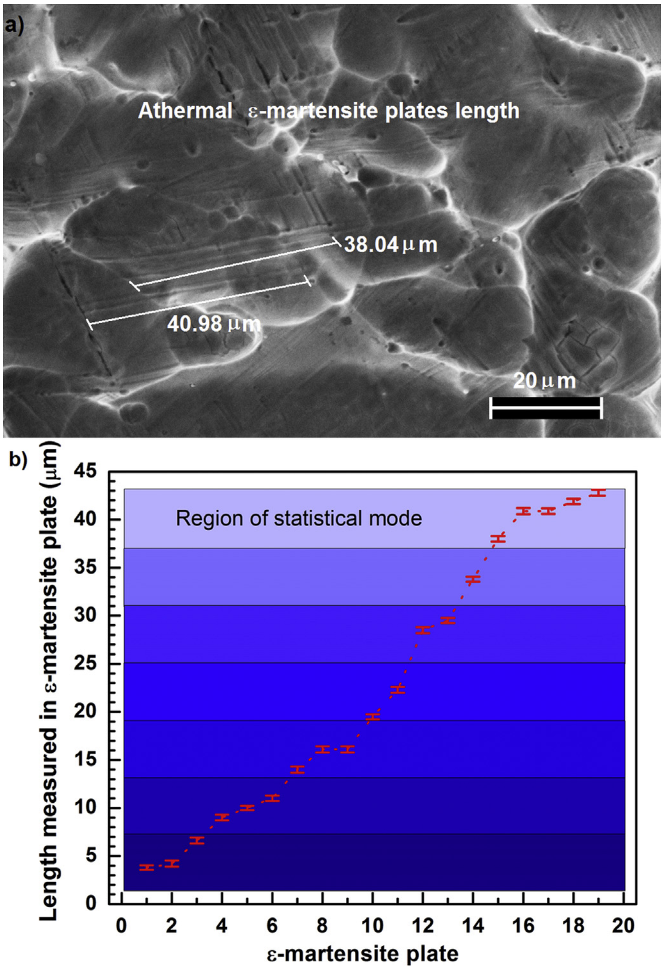

Fig. 11. (a) SEM micrograph of athermal ε-martensite plates and their sizes, (b) Length of ε-martensite plates measured in Fig. 11(a), graphic is divided on different regions in order to identify the region with statistical mode.

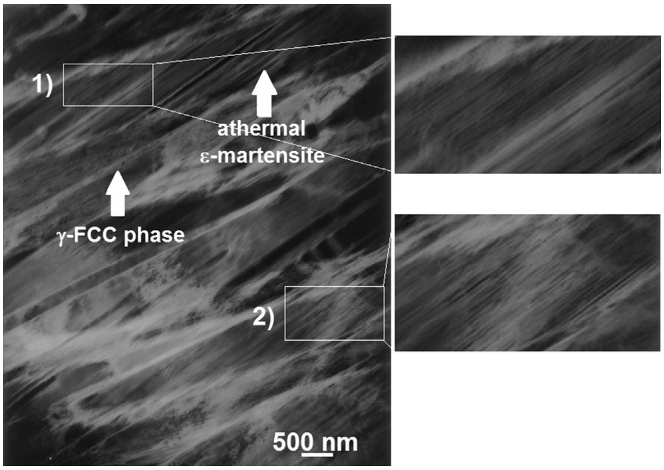

Fig. 12. TEM micrograph showing some residual γ-Co phase between fine martensite plates, as well as selected areas 1) and 2) containing large numbers of aligned athermal ε-martensite used for plate thickness measurements.

1.211×10^{-11} cm^3. Based on this value, the density of faulting defects that act a nucleation sites can be estimated yielding 8.258×10^{10} embryos/cm^3.

In addition, from the experimentally measured plate thickness the estimated number of extended dislocations in a given martensite plate is of the order of 16–17. This is at least twice the number of extended dislocations estimated by Olson and Cohen for critically sized martensite embryos. Apparently, under rapid solidification conditions, there is enough transformation energy to surmount the relatively high energy conditions required for spontaneous nucleation in this alloy. For comparative purposes, Table 2 contains the estimated energy barriers for nucleation including some corresponding to other alloy systems. Notice that in a conventionally solidified Co–29Cr–6Mo alloy (see Table 2), an estimation of the number of dissociated dislocations gives 3–4 which is close to the one predicted in the work of Olson and Cohen. The magnitudes of the alloy properties used for these determinations were extracted from the references given in the first column of this table.

From the above outcome, it is evident that the energy barrier and the critical plate dimensions are strongly influenced by ΔG_V. In particular, it is found that the magnitude of ΔG_V for the Co–20Cr is well below the ones reported for other alloy systems, including some Co-alloys [21,28,30,31]. Apparently, in the investigated cobalt alloy, there is a relatively high energy barrier for the martensite nucleation when compared with other systems. Nevertheless, a relatively high energy barrier favors an increase in the critical dimensions of the athermal martensite embryos and they agree with the experimental outcome of this work (see Table 2). Thus, it is evident that rapid solidification greatly enhances the spontaneous nucleation of ε-martensite embryos by increasing the density of faulting defects in the investigated alloy.

5. Conclusions

In the present work, experimental conclusive evidence is provided which indicates a drastic increase in the formation of athermal martensite by implementing chill casting in a Co–20Cr alloy. Rapid solidification was achieved with an alloy cooling rate of 278 K/s when casting in a water cooled Cu-mold was introduced. The estimated amount of precipitated athermal ε-martensite measured using X-ray diffraction was 97.26 vol. %. An examination of the exhibited microstructure including consideration of some mechanistic aspects associated with the transformation, particularly, martensite embryo nucleation yields the following:

1. Rapid solidification promotes appreciable dendrite grain refinement and alloy homogenization (i.e. nearly segregation free columnar dendrites, Fig. 10). In addition, numerous visible striations associated with the $\gamma \leftrightarrow \varepsilon$ transformation inside columnar dendrites indicated the dissociation of lattice dislocations along planes of closest packing (111) in the γ-Co FCC phase.
2. TEM observations indicated the development of an extremely large amount of stacking faults and stacking fault intersections, including ε-martensite plates.
3. Eshelby's inclusion theory was considered in estimating critical conditions in terms of energy and plate size conditions for spontaneous martensite embryo nucleation. The geometry of the martensite embryos was assumed to consist of thin ellipsoidal plates and their dimensions were experimentally determined by SEM and TEM means.
4. A comparison between the predictions of Eshelby's inclusion theory and the experimental outcome for plate dimensions indicates good agreement as the error involved is only 1.486% for plate length and 0.812% for plate thickness.
5. An estimation of the chemical volumetric free energy ΔG_V using a regular solution model indicated that the magnitude of this term is rather small when compared with other alloy systems. In turn, it is found that the energy barrier for spontaneous nucleation is relatively high resulting in appreciably large sized athermal martensite plates.

Acknowledgments

The authors gratefully acknowledge the technical support from A. Tejeda, C. Flores-Morales and C. Zorrilla, and the financial support from UNAM/PAPIIT IT100316.

Appendix A

Free energy estimation (ΔG_V)

An accurate estimation of the ΔG_V value for the Co–20Cr alloy can be obtained by following the method proposed by Allain and Co-workers [26]. In this method, the Gibbs free energy for the austenite-martensite transformation can be estimated using a regular solution model. Consider a Co–Cr binary system, undergoing an austenite-martensite transformation, with the molar Gibbs free energy given by Eq. (A1).

$$\Delta G^{\gamma\to\varepsilon} = \chi_{Co}\Delta G_{Co}^{\gamma\to\varepsilon} + \chi_{Cr}\Delta G_{Cr}^{\gamma\to\varepsilon} + \chi_{Co}\chi_{Cr}\Omega_{CoCr}^{\gamma\to\varepsilon} + \Delta G_{mg}^{\gamma\to\varepsilon}. \tag{A1}$$

The first two terms in the right hand side of this equation are the products of the molar fractions of the pure elements (χ_{Co} andχ_{Cr}) and their corresponding differences in molar Gibbs energies between austenite and martensite in paramagnetic pure elements ($\Delta G_{Co}^{\gamma\to\varepsilon} = (\Delta G_{Co}^{\varepsilon} - \Delta G_{Co}^{\gamma})$ and $\Delta G_{Cr}^{\gamma\to\varepsilon} = (\Delta G_{Cr}^{\varepsilon} - \Delta G_{Cr}^{\gamma})$). The molar Gibbs free energy also considers the net excess of molar Gibbs energy due to mixing elements in the austenite-martensite transformation ($\chi_{Co}\chi_{Cr}\Omega_{CoCr}^{\gamma\to\varepsilon} = (\Delta G_{m}^{\varepsilon} - \Delta G_{m}^{\gamma})$) and the difference of molar Gibbs energy at the magnetic transition ($\Delta G_{mg}^{\gamma\to\varepsilon} = (G_{mg}^{\varepsilon} - G_{mg}^{\gamma})$).

In the Co–20Cr alloy the molar fractions of the pure elements are χ_{Co}=6.7877 and χ_{Cr}=1.9234. Gibbs energies for pure elements as a function of temperature are extracted from thermochemical database of Scientific Group Thermodata Europe (SGTE) [41,42], where the $\gamma \to \varepsilon$ transition occurs at approximately 1098.15 K.

Expressions for excess Gibbs energy and Gibbs energy associated with the magnetic transition are obtained by Oikawa and Coworkers in Ref. [42]. Excess Gibbs energy determinations can be made by means of the Redlich–Kister description [42].

$$G_{mg} = RT\, ln(\beta + 1) f(\tau). \tag{A2}$$

The molar Gibbs energy at the magnetic transition as given by Eq. (A2) is a function of the transformation temperature (T), Bohr magneton number (β) and the polynomial function $f(\tau)$ whose argument is the ratio between T and the Curie temperature (T_C) [42].

From the above expressions, absolute $\Delta G^{\gamma\to\varepsilon}$ values were determined yielding 14.866 J/mol. Moreover, in order to obtain the corresponding ΔG_V value the equivalency described by Ferreira and Müllner in Ref. [25] was used. In their method they consider a conversion factor given by the volume of one mol of atoms.

In addition the volume of a HCP unit cell (V_{HCP}) can be estimated from the experimental outcome. According to the XRD patterns for the Co–alloy, the lattice parameter in the FCC cell (a_{FCC}) remains at

0.3464×10^{-9} m. Alternatively, in the HCP phase there is an observed contraction (s) normal to the basal plane when the $\gamma \rightarrow \varepsilon$ transformation occurs, this contraction in the c-axis is roughly 1.98%. Thus,

$$V_{HCP} = \left(\frac{a_{FCC}\sqrt{2}}{2}\right)^2 (1-s) = \left(\frac{a_{FCC}\sqrt{2}}{2}\right)^2 \left(\frac{2a_{FCC}}{\sqrt{3}}(1-0.00198)\right) = 2.353 \times 10^{-29}\left[m^3\right]. \quad \text{(A3)}$$

Eq. (A3) represents the volume of two atoms in the Co-Cr alloy [25]. Now, by considering the volume of one mol of atoms, the equivalence between $\Delta G^{\gamma \rightarrow \varepsilon}$ and ΔG_V is then given by

$$\Delta G_V = 141155 * \Delta G^{\gamma \rightarrow \varepsilon} \left[J/m^3\right]. \quad \text{(A4)}$$

References

[1] Q. Chen, G.A. Thouas, Metallic implant biomaterials, Mater. Sci. Eng. R. 87R (2015) 1–57.

[2] I. Milošev, CoCrMo alloy for biomedical applications, in: S.S. Djokić (Ed.), Biomedical Applications, Springer, London, 2012, pp. 1–72.

[3] K. Ishida, T. Nishizawa, The Co–Cr (Cobalt–Chromium) system, Bull. Alloy Phase Diagr. 11 (1990) 357–370.

[4] K.P. Gupta, The Co–Cr–Ta (Cobalt–Chromium–Tantalum) system, J. Phase Equilib. Diff. 26 (2005) 93–97.

[5] J.B. Vander-Sande, J.R. Coke, J. Wulff, A transmission electron microscopy study of the mechanisms of strengthening in heat-treated Co–Cr–Mo–C alloys, Metall. Trans. A 7A (1976) 389–397.

[6] A.J. Saldivar-Garcia, A. Mani-Medrano, A. Salinas-Rodriguez, Effect of solution treatments on the FCC/HCP isothermal martensitic transformation in Co–27Cr–5Mo–0.05C aged at 800°C, Scr. Mater. 40 (1999) 717–722.

[7] Y.P. Li, J.S. Yu, S. Kurosu, Y. Koizumi, H. Matsumoto, A. Chiba, Role of nitrogen addition in stabilizing the γ phase of Biomedical Co–29Cr–6Mo alloy, Mater. Chem. Phys. 133 (2012) 29–32.

[8] V. Raghavan, Kinetics of martensitic transformations, in: G.B. Olson, W.S. Owen (Eds.), Martensite. A Tribute to Morris Cohen, ASM International, USA, 1992, pp. 197–226.

[9] A.J. Saldívar-García, Doctoral Thesis CINVESTAV-ipn Unidad Saltillo, México, 1998.

[10] A.J. Saldívar-García, A. Mani-Medrano, A. Salinas-Rodríguez, Formation of hcp martensite during the isothermal aging of an fcc Co–27Cr–5Mo–0.05C orthopedic implant alloy, Metall. Mater. Trans. A 30A (1999) 1177–1184.

[11] N. Cong-Dahn, D. Morphy, K. Rajan, Kinetics of the martensitic f.c.c.→ h.c.p. transformation in Co–Cr–Mo alloy powders, Acta Metall. 32 (1984) 1317–1322.

[12] Y. Koizumi, Sh Suzuki, K. Yamanaka, B.S. Lee, K. Sato, Y. Li, Sh Kurosu, H. Matsumoto, A. Chiba, Strain-induced martensitic transformation near twin boundaries in a biomedical Co–Cr–Mo alloy with negative stacking fault energy, Acta Mater. 61 (2013) 1648–1661.

[13] P. Huang, A. Salinas-Rodriguez, H.F. Lopez, Tribological behaviour of cast and wrought Co–Cr–Mo implant alloys, Mater. Sci. Technol. 15 (1999) 1324–1330.

[14] G.B. Olson, M. Cohen, A general mechanism of martensitic nucleation: Part I. General concepts and the FCC→HCP transformation, Metall. Trans. A 7A (1976) 1897–1904.

[15] K. Rajan, Nucleation of recrystallization in a Co–Cr–Mo alloy, Metall. Trans. A 15A (1984) 1335–1338.

[16] H.F. Lopez, A. Saldivar, P. Huang, Development and properties of ε-martensite in Co–Cr–Mo alloys for biomedical applications, in: A. Meike, A. Gonis, P.E.A. Turchi, K. Rajan (Eds.), Properties of Complex Inorganic Solids 2, Kluwer Academic/Plenum Publishers, New York, 1999, pp. 307–325.

[17] L. Mingxi, H. Yizhu, S. Guoxiong, Microstructure and wear resistance of laser clad cobalt-based alloy multi-layer coatings, Appl. Surf. Sci. 230 (2004) 201–206.

[18] A. Chiba, N. Nomura, Y. Ono, Microstructure and mechanical properties of biomedical Co–29Cr–8Mo alloy wire fabricated by a modified melt-spinning process, Acta Mater. 55 (2007) 2119–2128.

[19] Sh Zangeneh, M. Ketabchi, H.F. Lopez, Nanoscale carbide precipitation in Co–28Cr–5Mo–0.3C implant alloy during martensite transformation, Mater. Lett. 116 (2014) 188–190.

[20] G. Barucca, E. Santecchia, G. Majni, E. Girardin, E. Bassoli, L. Denti, A. Gatto, L. Iuliano, T. Moskalewics, P. Mengucci, Structural characterization of biomedical Co–Cr–Mo components produced by direct metal laser sintering, Mater. Sci. Eng. C 48C (2015) 263–269.

[21] K.E. Easterling, A.R. Thölén, The nucleation of martensite in steel, Acta Metall. 24 (1976) 333–341.

[22] J.D. Eshelby, The determination of the elastic field of an ellipsoidal inclusion, and related problems, Proc. R. Soc. A 241A (1957) 376–396.

[23] G.B. Olson, M. Cohen, A general mechanism of martensitic nucleation: Part II. FCC→BCC and other martensitic transformations, Metall. Trans. A 7A (1976) 1905–1914.

[24] G.B. Olson, M. Cohen, A perspective on martensitic nucleation, Ann. Rev. Mater. Sci. 11 (1981) 1–30.

[25] P.J. Ferreira, P. Müllner, A thermodynamic model for the stacking-fault energy, Acta Mater. 46 (1998) 4479–4484.

[26] S. Allain, J.-P. Chateau, O. Bouaziz, S. Migot, N. Guelton, Correlations between the calculated stacking fault energy and the plasticity mechanisms in Fe–Mn–C alloys, Mater. Sci. Eng. A-Struct 387–389 (2004) 158–162.

[27] L. Rémy, A. Pineau, B. Thomas, Temperature dependence of stacking fault energy in close-packed metals and alloys, Mater. Sci. Eng. 36 (1978) 47–63.

[28] K. Yamanaka, M. Mori, S. Kurosu, H. Matsumoto, A. Chiba, Ultrafine grain refinement of biomedical Co–29Cr–6Mo alloy during conventional hot-compression deformation, Metall. Mater. Trans. A 40A (2009) 1980–1994.

[29] K. Yamanaka, M. Mori, A. Chiba, Nanoarchitectured Co–Cr–Mo orthopedic implant alloys: nitrogen-enhanced nanostructural evolution and its effect on phase stability, Acta Biomater. 9 (2013) 6259–6267.

[30] H.F. López, A.J. Saldivar-Garcia, Martensitic transformation in a cast Co–Cr–Mo–C alloy, Metall. Mater. Trans. A 39 (2008) 8–18.

[31] R.E. Stoltz, J.B. Vander Sande, The effect of nitrogen on stacking fault energy of Fe–Ni–Cr–Mn steels, Metall. Trans. A 11 (1980) 1033–1037.

[32] R. Kaiser, K. Williamson, C. O'brien, D.J. Browne, Effects of section size, surface cooling conditions, and crucible material on microstructure and as-cast properties of investment cast Co–Cr biomedical alloy, Metall. Mater. Trans. A 44 (2013) 5333–5342.

[33] M. Sage, C. Gillaud, Méthode d'analyse quantitative des variétés allotropiques du Cobalt pre les Rayons X, Rev. Metall. 49 (1950) 139–145.

[34] J.W. Edington, Monographs in Practical Electron Microscopy in Materials Science: Electron Diffraction in the Electron Microscope 2, Macmillan, Cambridge England, 1975.

[35] J.P. Hirth, J. Lothe, Theory of Dislocations, Krieger publishing company, Florida, 1991.

[36] K. Rajan, Phase transformations in a wrought Co–Cr–Mo–C alloy, Metall. Trans. A 13 (1982) 1161–1166.

[37] L.Z. Zhuang, E.W. Langer, Effects of cooling rate control during the solidification process on the microstructure and mechanical properties of cast Co–Cr–Mo alloy used for surgical implants, J. Mater. Sci. 24 (1989) 381–388.

[38] H. Jones, Rapid Solidification of Metals and Alloys, The institution of metallurgists, London, 1982.

[39] P. Huang, H.F. Lopez, Athermal ε-martensite in a Co–Cr–Mo alloy: grain size effects, Mater. Lett. 39 (1999) 249–253.

[40] H.R. Lashgari, Sh. Zangeneh, F. Hasanabadi, M. Saghafi, Microstructural evolution during isothermal aging and strain-induced transformation followed by isothermal aging in Co–Cr–Mo–C alloy: a comparative study, Mater. Sci. Eng. A 527A (2010) 4082–4091.

[41] A.T. Dinsdale, CALPHAD 15 (1991) 317.

[42] K. Oikawa, G.W. Qin, T. Ikeshoji, O. Kitakami, Y. Shimada, K. Ishida, K. Fukamichi, Thermodynamic calculations of phase equilibria of Co–Cr–Pt ternary system and magnetically induced phase separation in the FCC and HCP phases, J. Magn. Magn. Mater. 236 (2001) 220–233.